A Novel Anti-Interference Encapsulated 3-Bit Coded RFID Humidity Sensor Based on Bent Microstrip

Jingwen Hu, Yaming Xie, Guochun Wan, *Member, IEEE*, and Liyu Xie

Abstract*— This article proposed a 3-bit coded chipless radio frequency identification (RFID) humidity sensor that is anti-interference encapsulated. The proposed sensor is fed through a bent microstrip, and the sensing tag includes three split ring resonators (SRRs) as encoding bits and an interdigital-capacitor (IDC) structure covered with Kapton film as the humidity sensor, fabricated in a Rogers RO3003 dielectric substrate. A planar ultra-wideband (UWB) antenna with an operating frequency range of 1.88–6.04 GHz is proposed to be integrated with sensors as receiving and transmitting antennas. The sensor's humidity detection capability is attributed to the enhanced design of the IDC-sensing element, which is covered with a Kapton film whose dielectric constant varies with humidity, causing a change in the electromagnetic field, so that the sensor is capable of detecting small variations in the electromagnetic properties that characterize different humidities. In addition, humidity-insensitive polydimethylsiloxane (PDMS) is used as the encapsulating layer to minimize the interference of humidity on the coding bits and improve the life cycle. The performance of the fabricated sensor was verified using a vector network analyzer (VNA). The VNA recorded a clear frequency shift response at 23%–90% relative humidity (RH), with a humidity sensitivity of 396 kHz/%RH. Experiments were conducted to validate the repeatability, response time, and recovery time of the sensor measurement. The response time is about 60 s, and the recovery time is about 80 s. Through multiple experiments, it has been confirmed that the measurement accuracy can be maintained within the 30%RH–80%RH range. In addition to having an anti-interference encapsulated, the proposed humidity sensor also has several other advantages, including small size, simple fabrication, and low cost. The use of chipless RFID technology to achieve long-term humidity monitoring is of great significance in structural health monitoring (SHM).

***Index Terms*— Chipless radio frequency identification (RFID), encoding, humidity sensor, Kapton, sensing materials.**

I. INTRODUCTION

SMART sensing technologies are becoming increasingly important in structural health monitoring (SHM). As sensors face new demands, such as flexibility, reading sensor data wirelessly, high sensitivity, antienvironmental interference, and low cost, a variety of new sensors have emerged one after another. Among the emerging smart structural monitoring methods, tag antenna-sensing technology is attracting significant attention. Radio frequency identification (RFID) tag sensors have many applications and features that make them a hot research topic for the future [1]. RFID sensors can be used for structural health detection of various buildings under structural hazards (strain, cracks, and so on) and different environmental conditions (temperature and humidity), which will improve the safety of buildings. RFID tag-sensing technology also has many other application areas, such as human health monitoring [2], body area networks [3], liquid composition detection [4], and noninvasive glucose monitoring [5].

Among the various wireless sensors, RFID has rapidly gained success in the last few decades due to its low cost and the fact that it does not require a power supply in passive mode. RFID systems use tags that have no internal power source but are activated by electromagnetic energy transmission from the reader. The absence of electronic circuitry makes it cheaper and easier to mass produce [6]. Because there is no need to replace batteries and other maintenance work, RFID sensors have the advantage of long service life. If the sensor is placed in the main body of the building, it can detect for several years. Many studies use passive RFID tags as codes [7], and coding reconfigurability research [8], or as sensors to monitor various physical parameters, such as temperature [9], humidity [10], gas [11], strain [12], acceleration [13], displacement [14], or integrate multiple parameters [15]. RFID humidity sensors rely heavily on humidity-sensitive materials, which mainly include carbon-based materials, polyaniline [16], nonporous inorganic nanoparticles [17], composite compounds [18], polyimides [19], and paper-based materials [20]. Among these materials, some of them are covered on top of the metal radiating units, while others are used as substrates for the sensors. Some other hot research issues are the integration of sensors and microcontrollers to achieve more flexible and diverse detection methods, such as using a software-defined radio (SDR) device as a reader [21], sensor information fusion

Manuscript received 13 October 2023; revised 17 March 2024; accepted 25 March 2024. Date of publication 8 May 2024; date of current version 20 May 2024. This work was supported in part by the General Program of National Natural Science Foundation of China, "Research on the Principles of Passive Sensing and Structural Deformation Monitoring Methods Based on Antennas without Stress Patch" under Project 52078375; and in part by the Top Discipline Plan of Shanghai Universities-Class I. The Associate Editor coordinating the review process was Dr. Jose A. Gazquez. *(Jingwen Hu and Yaming Xie contributed equally to this work.) (Corresponding author: Guochun Wan.)*

Jingwen Hu, Yaming Xie, and Guochun Wan are with the Department of Electronic Science and Technology, Tongji University, Shanghai 200092, China (e-mail: 2132908@tongji.edu.cn; 2130800@tongji.edu.cn; wanguochun@tongji.edu.cn).

Liyu Xie is with the Department of Disaster Mitigation for Structures, Tongji University, Shanghai 200092, China (e-mail: liyuxie@tongji.edu.cn).

Digital Object Identifier 10.1109/TIM.2024.3398133

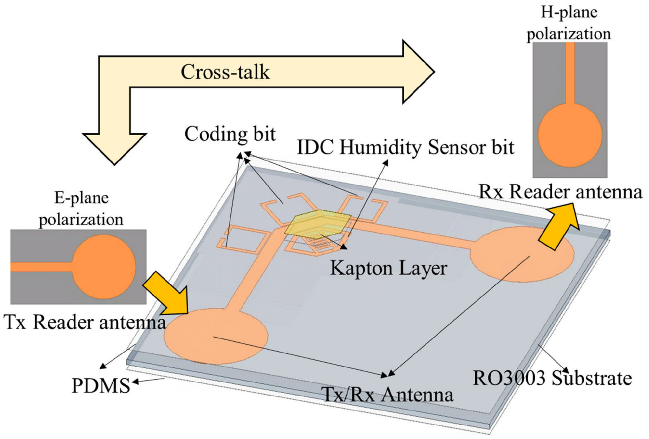

Fig. 1. Multiresonance chipless RFID system based on bent microstrip line.

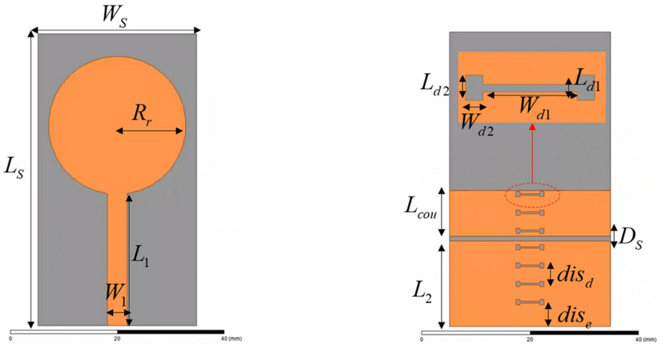

(a) (b)

Fig. 2. Schematic of structural parameters of circularly polarized UWB antenna: (a) radiation surface and (b) defect structure ground plane.

techniques [22], [23], and portable detection methods with integrated lightweight vector network analyzers (VNAs) [24]. RFID sensors allow measurements to be taken in a nonintrusive way, so they can be installed, for example, in harsh environments or hard-to-reach locations. The operating environment of mechanical equipment is usually harsh, and foreign objects, such as water, dust, and ice, in the environment will reduce the accuracy of RFID sensors [25]. During long-term monitoring, the copper layer of the antenna will react with oxygen, water vapor, and carbon dioxide in the air to form a patina. Therefore, it is necessary to design a sensor with an environmental interference encapsulation layer.

In this article, we proposed a 3-bit coding RFID humidity sensor based on frequency domain and using a planar circular polarization antenna as a transceiver antenna for communication, which has an anti-interference encapsulation layer. The tag part includes a humidity-sensing unit and 3-bit coding units, which are designed to be integrated with the ultra-wideband (UWB) communication transceiver antenna. The tag antenna sensor and the transceiver antenna are fabricated by the wet-etching method and use Kapton film as the humidity-sensing unit. The parts other than the sensing unit are covered with humidity-insensitive polydimethylsiloxane (PDMS) material to minimize the interference of ambient humidity and to improve the service life. The communication distance of the integrated tag sensor is measured experimentally. Finally, we verify the humidity-sensing performance of the sensor and confirm that the PDMS layer has an ameliorating effect on the environmental interference. The proposed encapsulation significantly improves the reliability of RFID sensors and has a wide range of engineering applications.

II. SENSING ARCHITECTURE

The proposed anti-interference encapsulated chipless humidity sensor consists of two parts: an integrated sensing tag antenna and a reader transmit–receive antenna, as shown in Fig. 1. The tag is a chipless antenna that encodes the frequency spectrum by introducing resonant frequency characteristics that correspond to data bits.

The Rx/Tx reader antenna obtains its frequency characteristics by interrogating the tag using a multifrequency signal. The tag is equivalent to a multiband filter, encoding its band-stop frequency characteristics into the frequency spectrum. Multiple resonators are cascaded, each resonator corresponding to a data bit in the tag. To provide isolation between transmitted and received signals, the reader and tag antennas are cross polarized to reduce crosstalk between them. The humidity-sensing resonator is coated with humidity-sensitive Kapton to achieve humidity sensing, and the resonator is designed as an IDC structure to increase the length of the structural bending and improve the sensitivity to humidity. The remaining part was covered with PDMS to isolate environmental interference and served as a variable control group with an outer protective layer.

III. TRANSCEIVER ANTENNA DESIGN BASED ON DGS STRUCTURE

This article proposes a UWB reader antenna based on a defective ground structure (DGS) with the dimensions of 55 × 30 mm. The proposed substrate for the communication antenna is Rogers RO3003 (dielectric constant $\varepsilon_r = 3$, and tan σ is 0.0013) with a thickness of 1.524 mm. The front radiating patch structure is shown in Fig. 2(a), where a circular patch with radius $R_r = 13$ mm is designed on the top surface of the substrate and connected to the 50-Ω microstrip feedline.

To increase the bandwidth, DGS is considered on the ground plane. It is obtained by etching away defective structures on the ground metal layer of the antenna. The DGS structure disturbs the distributed current on the ground plane through the defect structure on the ground plane, causing parameters to change, thereby designing an antenna with enhanced bandwidth. DGS is easier to manufacture than other technologies that increase bandwidth and gain. Typically, the geometry of a DGS consists of one or more slots. The ground plane is shown in Fig. 2(b), including a coupling slot and seven dumbbell-shaped slots on the plane of the DGS. The specific design parameters of the communication antenna are shown in Table I. The radius of the circular patch is calculated using the effective radius (1), and the effective radius is shown in (2) [26]

$$R_r = \frac{R_{\text{eff}}}{\left(1 + \frac{2h}{\pi \varepsilon_r R_{\text{eff}}}\left[\ln\left(\frac{1.57 R_{\text{eff}}}{h}\right) + 1.78\right]\right)^{\frac{1}{2}}} \tag{1}$$

TABLE I
UWB COMMUNICATION ANTENNA DESIGN PARAMETERS

Parameter	W_s	L_s	R_r	W_1	L_1	L_2	L_{cou}
Value (mm)	30	55	13	3.75	25	16	8.5
Parameter	W_{d1}	L_{d1}	W_{d2}	L_{d2}	D_S	dis_d	dis_e
Value (mm)	3.75	1	0.7	0.3	0.9	3.4	4.1

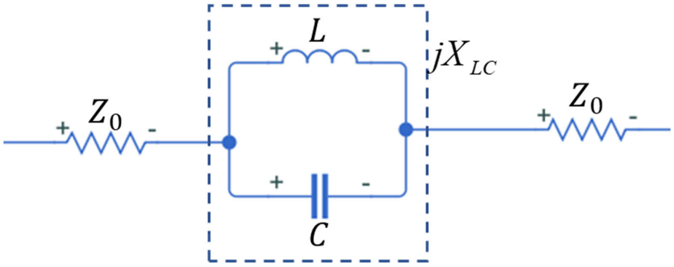

Fig. 3. Equivalent *LC* circuit prototype with dumbbell slots.

$$R_{\mathrm{eff}} = \frac{8.79 \times 10^9}{f_{\mathrm{res}}\sqrt{\varepsilon_r}} \tag{2}$$

where f_{res} represents the first resonant frequency, h represents the thickness of the substrate, and ε_r is the dielectric constant.

DGS is equivalent to an *LC* circuit using the lumped parameter method. Since the frequency characteristics of the dumbbell-shaped DGS are similar to the first-order single-pole Butterworth prototype filter, the circuit parameters are extracted using *LC* parallel theory. Fig. 3 illustrates the equivalent *LC* circuit prototype of a dumbbell-shaped DGS. The two internal resistances of the power supply and the circuit's output impedance are labeled as Z_0. Since a microstrip line with an impedance of 50 Ω is connected at both ends of the circuit, both Z_0 values are fixed at 50 Ω. The impedance of the *LC* parallel resonance loop is denoted as jX_{LC}.

The expression for the equivalent inductance can be derived from the resonance condition as follows:

$$L = \frac{1}{\omega_0^2 C} \tag{3}$$

where ω_0 is the corresponding resonance angular frequency value.

The impedance of the *LC* parallel resonant loop is [27]

$$X_{LC} = \frac{1}{\mathrm{j}}\left(\frac{1}{\mathrm{j}\omega C + \frac{1}{j\omega L}}\right) = \frac{1}{\frac{\omega_0^2 C}{\omega} - \omega C}. \tag{4}$$

The equivalent capacitance can be obtained from (3) and (4), which ω_c is the cutoff angular frequency with 3-dB attenuation

$$C = \frac{\omega_C}{2Z_0}\frac{1}{\omega_0^2 - \omega_C^2}. \tag{5}$$

The design of the antenna is simulated using Ansys high-frequency structure simulator (HFSS), an electromagnetic field simulation software developed by Ansys, which employs the finite-element method for calculations. The designed antenna underwent an evolutionary process, resulting in three schematics of grounded structures with defects and their corresponding electric field distribution simulations in Ansys HFSS, as illustrated in Fig. 4.

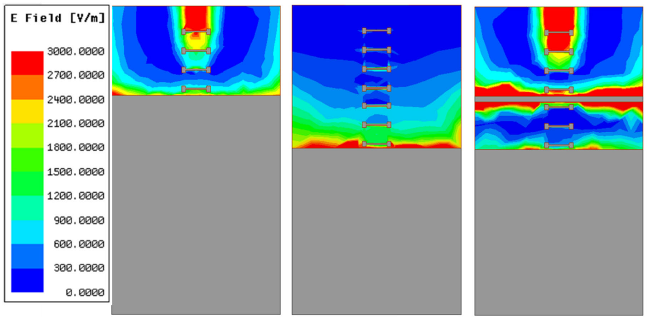

(a) (b) (c)

Fig. 4. Electric field distribution of three different ground plane designs: (a) Antenna 1, (b) Antenna 2, and (c) Antenna 3.

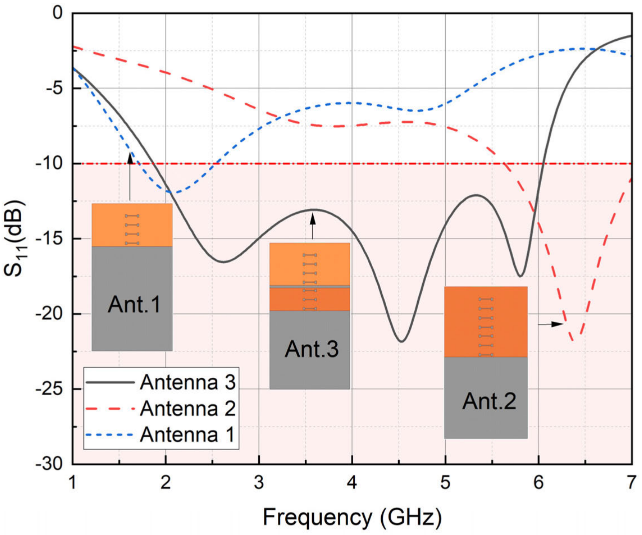

Fig. 5. S_{21} results for three antenna designs in Ansys HFSS.

The designs of Antenna 1 and Antenna 2 ultimately converged to form the design of Antenna 3. The distinction between Antenna 1 and Antenna 2 lies in the length of the ground plane covering the microstrip line on the radiating surface. For Antenna 1, only four dumbbell-shaped slots in the ground plane are considered, while Antenna 2 has seven dumbbell-shaped slots. The evolution from Antenna 2 to Antenna 3 involved the use of a ground plane slot to achieve increased bandwidth. The S_{11} of Antenna 1 is less than −10 dB between the 1.5 and 2.5 GHz bands. Antenna 2 considers seven dumbbell-shaped slots that are in 5.5–7.5 GHz. It can be seen that the resonance frequency changes, and the gain increases from the first evolution to the second one, from about −12.5 to −22.5 dB. Antenna 3 consists of seven dumbbell slots and a centerline coupling slot. S_{11} of Antenna 3 is 1.88–6.04 GHz, and the simulation is also shown in Fig. 5, using the −10 dB reference line to compare the bandwidth.

The desired UWB performance can be achieved by the design of Antenna 3. The gain radiation pattern obtained is shown in Fig. 6. It can be seen that the gain of the antenna

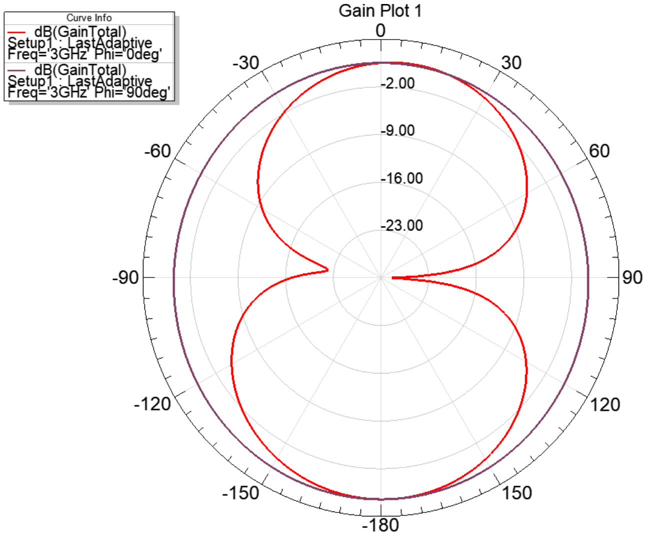

Fig. 6. *E*-plane and *H*-plane gain plots of Antenna 3.

is higher in the opposite direction and can only be read when the directions match.

IV. Sensing Tag Antenna Design

The proposed antenna design aims to integrate the 3-bit encoding unit and the humidity-sensing unit into the tag antenna part. To achieve miniaturization and meet the orthogonality required to connect transmit and receive antennas, the design will include encoding units, bent microstrip line structures, and IDC structures. The curved microstrip line ensures orthogonal polarization of the transmit and receive signals. The coding unit will consist of three resonators, each tuned to a unique frequency to encode 3 bits of data. The IDC humidity-sensing structure will be integrated into the tag, including the radiation conductor part and the humidity-sensing dielectric layer.

A. Design of Coding Units

In this study, a split resonator ring coupled to a microstrip line is used as the encoding unit, as shown in Fig. 7. The encoding principle is defined as 1 when there is a notch in the filter response and 0 otherwise. The resonator frequency is related to the length of the entire split ring resonator (SRR) and is calculated from its size parameters as follows:

$$L_{\text{total}} = L_{\text{out}} \cdot 4 - W_{\text{res}} \cdot 4 - \text{slot}_y. \tag{6}$$

The length and resonant frequency of the resonator were studied by simulation using Ansys HFSS. The total length of the resonator is 35 mm when $L_{\text{out}} = 10$ mm, $W_{\text{res}} = 1$ mm, and $\text{slot}_y = 1$ mm, and the resonant frequency obtained is 2.9 GHz. The sweeping simulation is performed by varying the width of the open slots, and the results are shown in Fig. 8(a). A curve fitting analysis was performed to match the length of the resonator and the corresponding resonant frequency point, and the fit curve is shown in Fig. 8(b), and the equation is as $F_r = -0.09905 \cdot L_{\text{total}} + 6.405$.

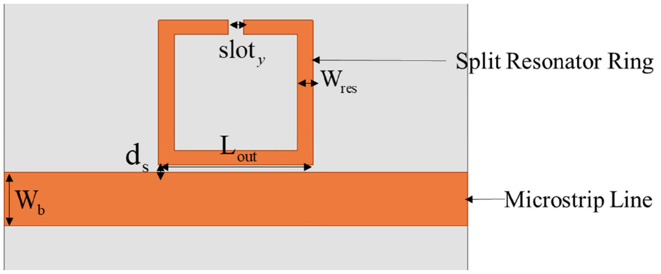

Fig. 7. Schematic of structural parameters of microstrip line-fed split resonant ring.

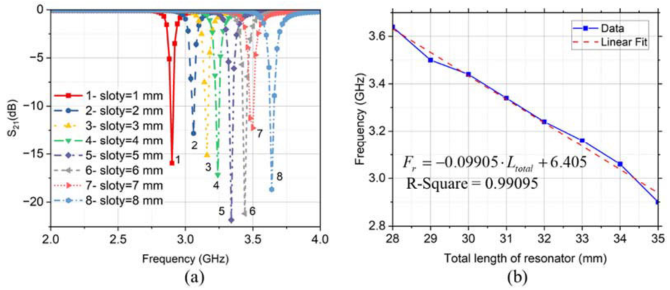

(a) (b)

Fig. 8. Length of slot in Ansys HFSS: (a) S_{21} results and (b) linear relationship between SRR length and resonant frequency.

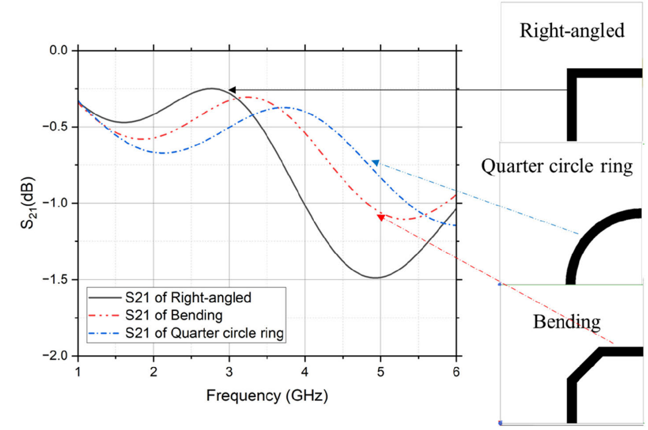

Fig. 9. S_{21} of three microstrip line structures in 1–6 GHz.

B. Bending Microstrip Line Structure

Most of the existing literature on microstrip line research focuses on straight-line structures. In this article, considering the two ports of the tag antenna that will be connected to the transmitter and receiver antennas, respectively, they need to be orthogonal to achieve high isolation. Therefore, the two ports need to be positioned along adjacent edges of the substrate. In microstrip line designs based on adjacent edges, three shapes are considered: right-angled, bending, and quarter-circle arcs. The schematics and S_{21} results of the three shapes of bent lines are shown in Fig. 9, and the shape with the smallest and most stable average loss is the bent line shape in the frequency range of 1–4 GHz, which is, therefore, chosen as the transmission line shape.

In microstrip lines, signals pass through the conductor portion, and the right-angled bend region may result in higher current density and concentration of electromagnetic fields. This may lead to resistive losses in the metal portion, converting a portion of the signal energy into heat and causing conductor losses. In addition, right-angled introduces radiation losses, where signal energy is radiated into space. This is due to the electromagnetic field's discontinuity at the right-angled bend, resulting in radiation energy loss [28]. The encoding design requires the microstrip lines to be arranged in coupling with the resonator. In the right-angled microstrip line design, there is a lack of space to encode bits on both sides of the microstrip line in the right-angled turn portion. This makes the design of right-angled microstrip lines require a larger area to achieve the same encoding bits. A solution is to adopt a smaller bend radius. Reducing the bend radius helps minimize conductor losses and mitigate the electromagnetic field's discontinuity. Therefore, considering quarter-circle ring microstrip lines, this design results in poor coupling between the annularly bent microstrip lines and the SRR resonator due to uneven distances between the microstrip lines and the SRR resonator, making it challenging to control the coupling area, thus complicating the calculation of the coupling coefficient. Through theoretical discussions, it is observed that a right-angled structure introduces significant losses at the turning point due to excessive bending. On the other hand, a quarter-circle arc shape results in a shorter total length of the microstrip line, reducing its efficiency. Both structures are unfavorable for the compactness of frequency-domain encoding. Therefore, considering the balance between energy losses and coupling with encoding resonators, we propose this three-segment bend line microstrip line structure.

C. Design of IDC Structured Humidity-Sensing Tag

A humidity-coupled coding bit is designed based on the structure of an interdigital capacitor (IDC). The bent structure of the IDC unit is used to increase the effect of the dielectric constant of the humidity-sensitive layer on the antenna's performance by forcing the RF signals to travel longer inside the substrate. The resonant frequency of the proposed design is targeted at 2.26 GHz. The operating principle of the humidity-sensing unit is based on the properties of Kapton. Humidity-sensitive Kapton is used in conjunction with relative humidity (RH) sensing. As polyimide absorbs water, the dielectric constant changes, which is linearly related to the surrounding RH. According to Kapton's datasheet, when the RH increases from 0%RH to 100%RH, Kapton's relative dielectric constant changes from 3.05 to 3.9 [1]. Due to the propagation of electromagnetic waves in the air and different media, based on the humidity-sensitive properties of Kapton, it is suggested that the Kapton material adheres to the surface of the IDC structure. The change in the dielectric constant of Kapton film after absorbing water will be transferred to the change in the antenna electromagnetic field, which will result in the change of resonance frequency of the IDC structure. By relating the dielectric constant of the substrate to the best matching frequency, the RH can be related to the relative dielectric constant of Kapton by the following equation:

$$\%\mathrm{RH} = \frac{\varepsilon_r - 3.05}{0.008}. \tag{7}$$

In summary, the parameters of the simulation structure diagram for the overall coding and humidity tag are designed, as shown in Fig. 10, and the specific parameters are shown in Table II. The electric field distribution is shown in Fig. 11, where Fig. 11(a) is excited at 2.26 GHz, Fig. 11(b) is excited at 2.64 GHz, Fig. 11(c) is excited at 2.78 GHz, and Fig. 11(d) is excited at 2.92 GHz. It can be seen that only one sensing coding bit is excited at 2.26 GHz, and three coding bits are excited at 2.64, 2.78, and 2.92 GHz, respectively.

TABLE II
CODING AND HUMIDITY TAG SENSOR PARAMETERS

Parameter	S_{out}	S_{slot}	M_{out}	M_{slot}	L_{out}	L_{slot}
Value (mm)	10.45	2	10.9	2.25	11.85	3.25
Parameter	wid	d	W_b	d_{IDC}	w_{IDC}	l_h
Value (mm)	1	0.3	3.73	0.36	0.84	11.9

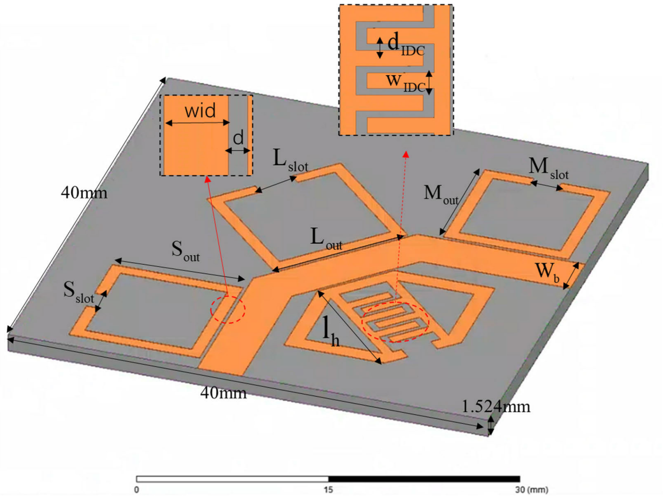

Fig. 10. Schematic of the parameters of the simulated structure of the overall encoding and humidity tag.

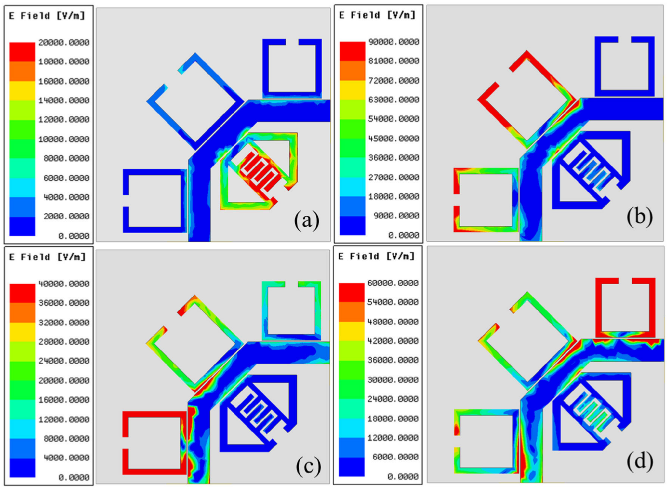

Fig. 11. Overall coded and humidity tag's electric field distribution at different frequencies: (a) 2.26, (b) 2.64, (c) 2.78, and (d) 2.92 GHz.

V. SENSOR CHARACTERIZATION EXPERIMENT AND ANALYSIS

In this work, a wet-etch fabrication method was used to fabricate the antenna to verify the measurements.

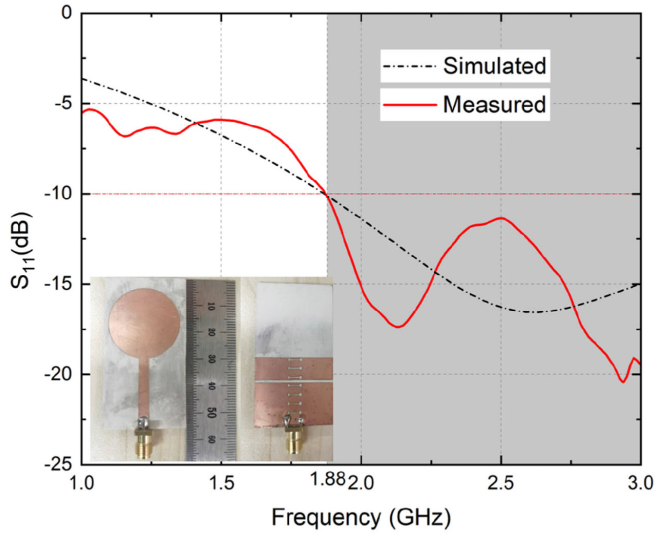

Fig. 12. Photographs and measurements of the fabricated circularly polarized UWB antenna.

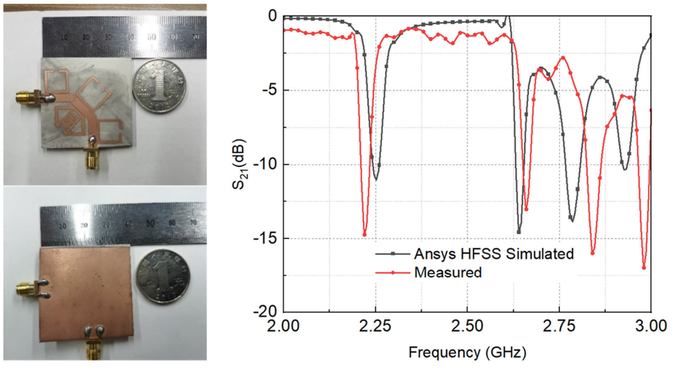

(a) (b)

Fig. 13. Fabricated tag: (a) photograph and (b) simulation and measurement results.

The reflection coefficient (S_{11}) was measured using the Rohde and Schwarz ZVL VNA. Photographs and measurements of the fabricated circularly polarized antenna are shown in Fig. 12. The measured results are similar to the simulated results with slight differences due to fabrication errors and the effect of the coaxial cable used for the measurements. As described in Section II, the simulated S_{11} covers a bandwidth of 4.16 GHz (1.88–6.04 GHz) with S_{11} greater than 10 dB and voltage standing wave ratio (VSWR) less than 2. The obtained bandwidth is useful for many wireless applications [29]. The proposed antenna shows good agreement between simulation and measurement results in the range of 1–3 GHz (the measurement range is limited to less than 3 GHz due to the limitation of VNA).

Photographs and measurements of the fabricated tag antenna are shown in Fig. 13. It can be seen that the measured resonance frequency of the humidity-sensing unit is 2.226 GHz, and the resonance frequencies of the 3-bit code are 2.66, 2.84, and 2.98 GHz in Fig. 13(b), which are similar to the simulated results but with slight differences due to manufacturing errors and the effect of the coaxial cable used for the measurements.

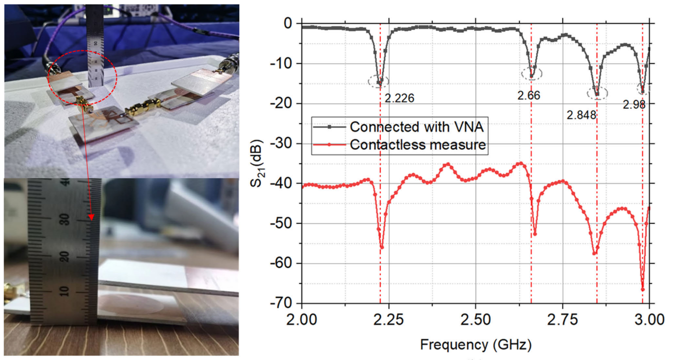

(a) (b)

Fig. 14. Contactless readout testing: (a) testing environment and (b) S_{21} results for direct connect and contactless readout.

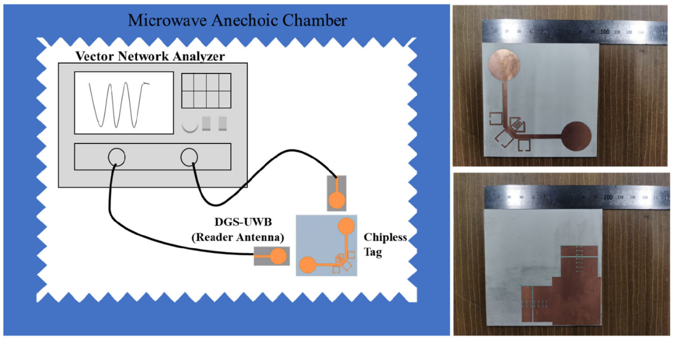

(a) (b)

Fig. 15. Integrated sensing tag measurements: (a) schematic of the microwave anechoic chamber measurement and (b) front and back of the physically integrated tag fabricated.

A. Contactless Readout Measurement

The sensor was connected directly to the VNA or connected to the UWB antennas by SMA (SubMiniature Version A) adapters to verify the feasibility of contactless reading. The testing environment and results are shown in Fig. 14.

An integrated sensor was fabricated using wet etching and tested for sensing distance. The test setup in the microwave anechoic chamber is shown in Fig. 15(a), and the tag is shown in Fig. 15(b). As shown in Fig. 16, the received frequency of the sensor was accurately detected at distances ranging from 10 to 120 mm. At a distance of 120 mm, the coded tag received 1 bit of false coding from the spurious interference, indicating that the effective receiving distance is less than 120 mm.

B. Humidity-Sensing Experiment

The humidity sensor with Kapton but not covered with PDMS was experimentally verified, and the sensor performance was measured in a humidity chamber, and the internal RH range is 23%–90%. For each test, the sensor was placed in the humidity chamber for a few minutes to allow the Kapton to absorb sufficient water, and then, the sensor's backscatter performance was quickly measured. During the entire measurement process, the laboratory temperature did not change by more than 1 °C, and the sensor position remained unchanged. Therefore, all changes in the curves

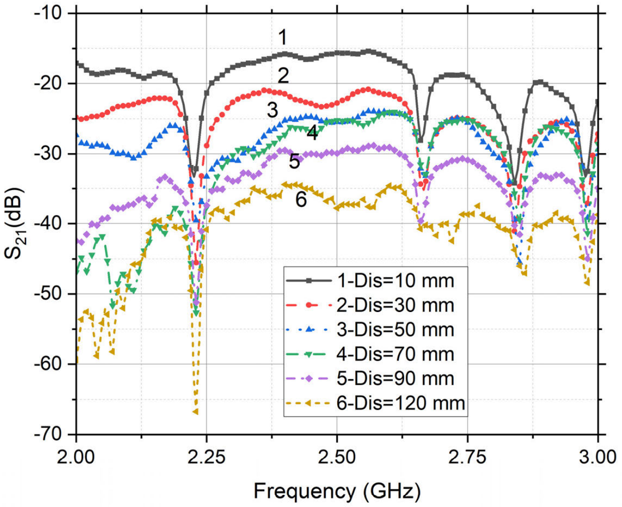

Fig. 16. Contactless readout distance test of integrated tags.

(a) (b)

Fig. 17. Photographs of microwave anechoic chamber testing scenarios: (a) microwave anechoic chamber environment and (b) inside the humidity chamber.

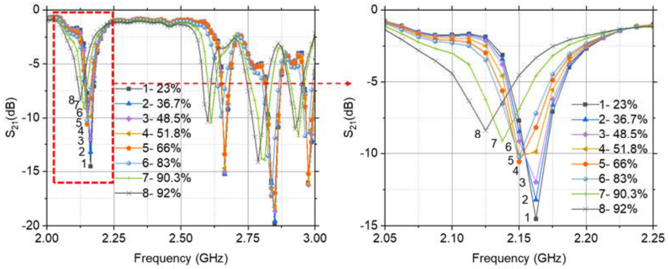

(a) (b)

Fig. 18. S_{21} test results for different RH environments: (a) 2–3 and (b) 2.05–2.25 GHz for humidity-sensing unit.

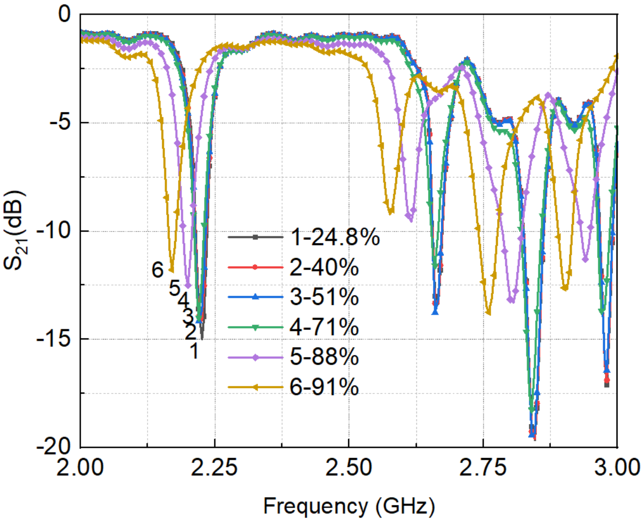

Fig. 19. Measurements under changing humidity conditions without Kapton film coverage.

can be considered to be caused by changes in the electrical parameters of the Kapton layer. The experimental setup and results are shown in Fig. 17. The humidity chamber is a self-made simplified humidity chamber, with its composition depicted in Fig. 17(b). This chamber is a sealed foam box and is internally equipped with a humidifier consisting of a container, cotton swab filter core, and a portable charger. In addition, it contains calcium chloride (facilitating a more rapid reduction of the required humidity inside the chamber). The internal dimensions measure 27 × 24 × 20 cm^3. The selected commercial hygrometer is the SMART SENSOR AR847 + digital hygrothermometer. Due to the presence of a connecting cable between the digital display and the temperature-humidity sensor of the hygrometer, the sensor is positioned within the sealed humidity chamber, while the digital display is located externally. The region through which the connecting cable passes is sealed using adhesive tape. Subsequently, the humidity sensor designed in this study is connected to a BNC to SMA cable, with one part of the cable inside the humidity chamber and the other part outside, connected to the VNA. Fig. 18 illustrates measurements in the 2–3 GHz under different humidities. The humidity was raised to 90%, and then, the sensor was placed in a normal indoor environment (winter in Shanghai, 23% humidity and 25 °C).

It can be seen from the experimental results that in addition to the humidity-sensing unit, there is also a deviation in the encoding position. This may be because the substrate has certain water-absorbing properties, which will interfere with the experiment. To compare with the substrate without Kapton film, we conducted a comparative experiment and obtained the results shown in Fig. 19. It is difficult to achieve appropriate decoupling to eliminate interference. Therefore, consider covering other parts of the substrate with a hydrophobic PDMS film to isolate environmental interference.

C. Anti-Interference PDMS Encapsulation Layer

This article proposes an anti-interference encapsulation layer for RFID sensors. The encapsulation layer uses PDMS with humidity-insensitive characteristics, which greatly reduces the level of fluctuations in the resonant frequency caused by changes in humidity. The photograph of the sensor after covering the PDMS is shown in Fig. 20(a), and the S_{21} results are shown in Fig. 20(b). The fit plot of frequency and humidity is shown in Fig. 21, and the equation is $F_2 = -3.96532e^{-4}\ H_r + 2.16793$, where F_2 is the resonance frequency (GHz) and H_r is the humidity. This gives a humidity sensitivity of approximately 396 kHz/%RH. It can be observed that the resonant frequency of the three encoding bits hardly changes with humidity. During the experiment, the temperature in the chamber was maintained at about 25 °C. Experimental results show that the proposed method of using

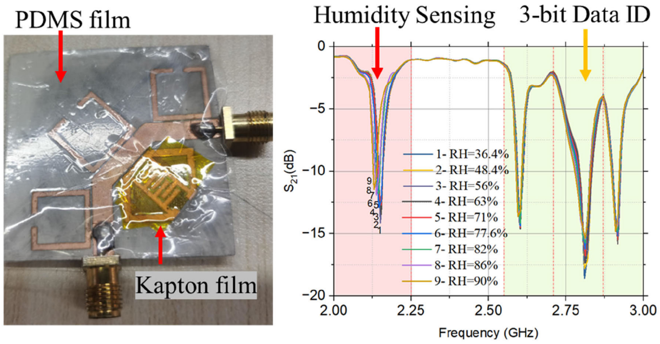

(a) (b)

Fig. 20. Humidity-sensing measurements after covering PDMS: (a) physical schematic and (b) S_{21} results in 2–3 GHz.

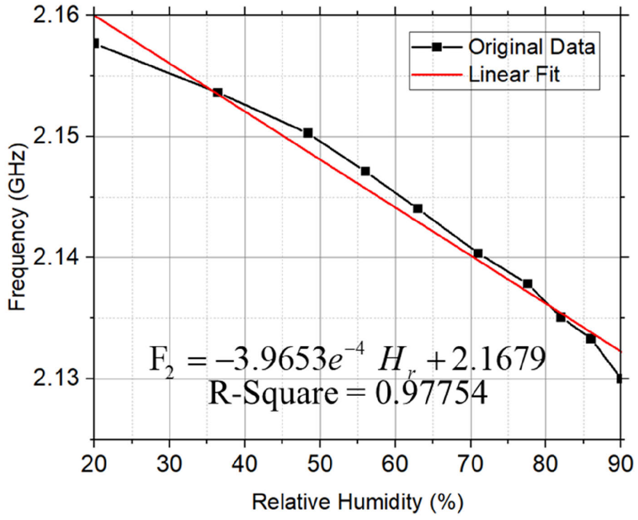

Fig. 21. Linear fit of RH to the resonant frequency at a constant temperature of 25 °C.

antenna encapsulation technology to resist interference from environmental foreign objects greatly improves the reliability of the humidity sensor, but also reduces the sensitivity of the sensor accordingly.

D. Response and Recovery Time

Due to the repetitiveness required for humidity sensing, it is necessary to conduct multiple measurement experiments on the humidity-sensing component and test the response time and recovery time of the sensor. In the response time test, the humidity within the humidity chamber was elevated to 90%, and the sensor was placed in the chamber to record the response time. Subsequently, the sensor was placed in a normal indoor environment (23%RH and 25 °C), and the resonant frequency was allowed to return to its initial value. During this period, the resonant frequency, response time, and recovery time were regularly recorded, with a total time of 1200 s, and we conducted several experiments to verify its stability. In Fig. 22(a), the humidity sensor remains stable during multiple consecutive experiments, but the overall frequency decreases after multiple trials. Fig. 22(a) and (b) indicates that the humidity sensor completes its response in approximately 60 s on average. However, due to the continued absorption of moisture by the humidity-sensing material, there is still a slight frequency deviation. Therefore, this humidity sensor may cause its data to be inaccurate if it is exposed to high humidity for a long period. Then, there is the recovery experiment, and the sensor recovers to the normal resonant frequency in approximately 80 s and remains stable thereafter.

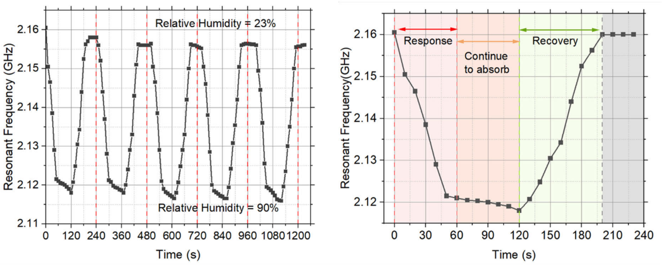

(a) (b)

Fig. 22. Response and recovery time test experiments for the designed humidity sensor: (a) multiple cycles within the 1200 s and (b) single cycle.

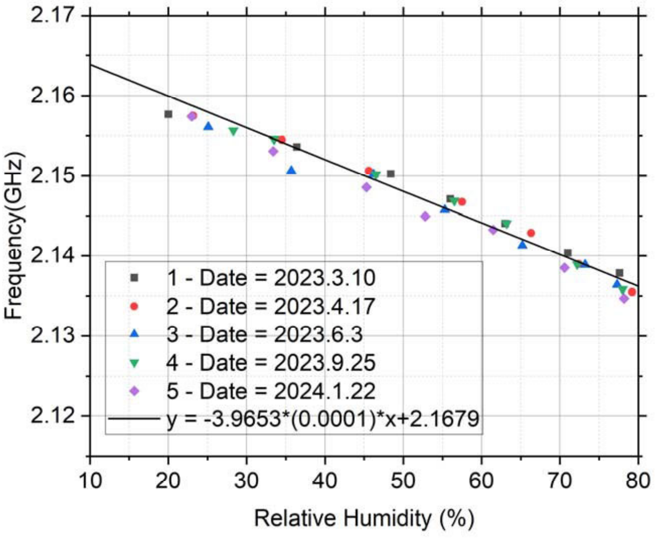

Fig. 23. Comparison of multiple data measurements and fitting equation.

We conducted multiple tests on RFID humidity sensors with PDMS film coating, and the humidity tests were carried out at intervals of several months, with the measurement charts shown in Fig. 23. The performance of the sensor remains stable in data separated by several months. The fitting equation is consistent when the humidity is 30%RH–80%RH. It shows that the sensor shows stability in multiple experiments, and long-term placement has little impact on sensor performance degradation.

Table III illustrates the literature reports on different types of humidity sensors. From various sensor types, it is observed that SAW sensors are not conducive to contactless reading and encoding, while *LC* and RFID types exhibit similarities. In the comparison of RFID humidity sensors, some literature lacks encoding functionality in their designs. Certain works, such as [19], [32], and [34], employ horn antennas for contactless reading. In contrast to the flat UWB antenna designed in this article, horn antennas have a higher cost, but their

TABLE III
HUMIDITY SENSOR COMPARED WITH OTHER STUDIES

Type	Range (%RH)	Sensitivity (/%RH)	Contactless Readout	Readout Antenna	Encoding Bits	Encoding bits anti-interference	Sensing Material	Ref.
RFID	11-98	2.95 MHz	No	-	3	No	SnO2/G	[18]
RFID	30-100	2 MHz	Yes	Horn Antenna	11	No	Polyimide	[19]
RFID	20-70	600 kHz	Yes	Loop Antenna	-	No	Paper substrate	[20]
SAW	0-90	70.6 kHz	No	-	-	No	3DAG/PVA /SiO2	[30]
LC	10-95	76.04 kHz	Yes	Loop Antenna	-	No	MoS2	[31]
RFID	30-90	4.8 MHz	Yes	Horn Antenna	3	No	SiNWs	[32]
RFID	0-90	1.5-3.9 MHz	No	-	-	No	Nafion 117	[33]
RFID	35-85	6.75 MHz	Yes	Loop Antenna	-	No	Polyvinyl-alcohol (PVA)	[34]
RFID	30-80	396 kHz	Yes	Planar Antenna	3	Yes	Polyimide	This paper

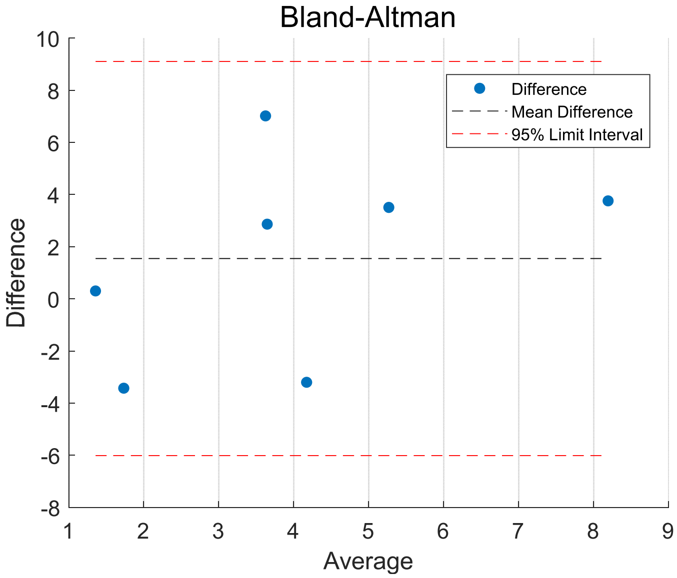

Fig. 24. Bland–Altman plot of the difference values of humidity estimates for humidity sensors designed in this article and [18].

advantage lies in an extended detection range. The cost of a horn antenna is approximately 5000 CNY each, requiring two for detection, whereas the cost of manufacturing a flat UWB antenna using wet etching (as in this article's design) is approximately 0.1–10 CNY each, varying depending on specific circumstances. While the humidity sensor proposed by [20] utilizes paper-based silver inkjet printing, and using a circular antenna for reading incurs lower costs, the long-term performance of paper-based materials and silver inkjet printing needs further discussion. Moreover, some literature employs humidity-sensitive materials that are complex and laboratory prepared, demanding high-production processes and costs, thus resulting in higher overall expenses. However, when considering the cost of comparing the VNAs of the testing instruments, the authors of each paper used different hardware, such as the brand and accuracy of the measuring instruments. Finally, from the table, it is evident that the design presented in this article features a unique encoding anti-interference encapsulation layer.

In this article, a Bland–Altman analysis is performed to compare the error of the humidity sensor designed in the previous literature [18] with the error of the humidity sensor in this article. The samples are the errors of the measured humidity and the estimated humidity from the fit equations for different humidity ranges. As shown in Fig. 24, the scatter points are distributed on both sides of the center line, and although there is a little deviation from the center line, it is within the acceptable range of the 95% limit interval. This indicates that the results of the measurement errors of the two methods are consistent at the average level.

VI. CONCLUSION

In this article, a low-cost chipless RFID-encoded humidity sensor based on a bent microstrip line with an encapsulation layer is proposed. The 3-bit coding unit is a microstrip resonant structure, where humidity sensing is realized by covering the humidity-sensitive Kapton, while the humidity-insensitive PDMS is used to cover the portion of the unit outside the sensing unit, to minimize the interference of humidity with the frequency-domain coding, and to improve the stability of the sensor coding. The integrated design and experimental validation were realized on a Rogers RO3003 substrate, and the expected performance of the fabricated sensor was practically verified using a VNA. An approximate linear relationship between the resonant frequency of the sensor and humidity was confirmed with a humidity sensitivity of 396 kHz/%RH for humidity variations from 30% to 80%. The transceiver antenna is a planar UWB circularly polarized antenna, which implements an integrated sensor design for contactless readout. In addition, we experimentally tested the communication distance of contactless reads within 120 mm for integrated tag sensors and verified that the PDMS encapsulation layer improves environmental interference. Our study shows that the use of a bent microstrip line structure is more favorable for the realization of contactless RFID humidity-encoded sensors, while the PDMS encapsulation technique improves the encoding stability of microstrip antenna sensors, which is of wide engineering applications in long-term environmental monitoring. Therefore, this coded humidity sensor should be used for long-term SHM by integrating coding to ensure unique identification between sensors. It can also be combined with strain sensing to form a multiparameter sensor. When applied to large building structures in the future, the sensor can be accurately positioned in complex sensor networks, effectively avoiding problems caused by sensor position ambiguity. However, there are still some shortcomings in this article, such as the adhesive properties of hybrid Kapton and PDMS films need to be improved in future studies.

REFERENCES

[1] J. Virtanen, L. Ukkonen, T. Bjorninen, and L. Sydanheimo, "Printed humidity sensor for UHF RFID systems," in *Proc. IEEE Sensors Appl. Symp. (SAS)*, Limerick, Ireland, Feb. 2010, pp. 269–272, doi: 10.1109/SAS.2010.5439426.

[2] D. Pardo et al., "Design criteria for full passive long range UHF RFID sensor for human body temperature monitoring," in *Proc. IEEE Int. Conf. RFID*, Grapevine, TX, USA, Mar. 2007, pp. 141–148, doi: 10.1109/RFID.2007.346162.

[3] I. Bouhassoune, R. Saadane, and A. Chehri, "Wireless body area network based on RFID system for healthcare monitoring: Progress and architectures," in *Proc. 15th Int. Conf. Signal-Image Technol. Internet-Based Syst. (SITIS)*, Sorrento, Italy, Nov. 2019, pp. 416–421, doi: 10.1109/SITIS.2019.00073.

[4] S. Bhushan, S. Kumar, N. Singh, and S. Kumar, "Defected ground split ring resonator-based sensor for adulteration detection in fluids," *Wireless Pers. Commun.*, vol. 121, no. 3, pp. 1593–1606, Dec. 2021, doi: 10.1007/s11277-021-08686-8.

[5] Y. Mahnashi, K. K. Qureshi, A. A. Al-Shehri, and H. Attia, "Design and experimental validation of a noninvasive glucose monitoring system using RF antenna-based biosensor," *IEEE Sensors J.*, vol. 23, no. 3, pp. 2856–2864, Feb. 2023, doi: 10.1109/JSEN.2022.3227382.

[6] K. Mekki, O. Necibi, H. Dinis, P. Mendes, and A. Gharsallah, "Frequency-spectra-based high coding capacity chipless RFID using an UWB-IR approach," *Sensors*, vol. 21, no. 7, p. 2525, Apr. 2021, doi: 10.3390/s21072525.

[7] S. Preradovic and N. C. Karmakar, "Multiresonator based chipless RFID tag and dedicated RFID reader," in *IEEE MTT-S Int. Microw. Symp. Dig.*, Anaheim, CA, USA, May 2010, pp. 1520–1523, doi: 10.1109/MWSYM.2010.5515168.

[8] G. Wan, Z. Jiang, and L. Xie, "A multiparameter integration method and characterization study of chipless RFID sensors with spiral shape," *IEEE Trans. Instrum. Meas.*, vol. 72, pp. 1–11, 2023, doi: 10.1109/TIM.2023.3306820.

[9] M. Bhattacharjee, F. Nikbakhtnasrabadi, and R. Dahiya, "Printed chipless antenna as flexible temperature sensor," *IEEE Internet Things J.*, vol. 8, no. 6, pp. 5101–5110, Mar. 2021, doi: 10.1109/JIOT.2021.3051467.

[10] P. Fathi, S. Bhattacharya, and N. C. Karmakar, "Dual-polarized keratin-based UWB chipless RFID relative humidity sensor," *IEEE Sensors J.*, vol. 22, no. 3, pp. 1924–1932, Feb. 2022, doi: 10.1109/JSEN.2021.3135500.

[11] A. Kumar and N. P. Pathak, "Wireless monitoring of volatile organic compounds/water vapor/gas pressure/temperature using RF transceiver," *IEEE Trans. Instrum. Meas.*, vol. 67, no. 9, pp. 2223–2234, Sep. 2018, doi: 10.1109/TIM.2018.2810718.

[12] G. Wan et al., "Separating strain sensor based on dual-resonant circular patch antenna with chipless RFID tag," *Smart Mater. Struct.*, vol. 30, no. 1, Jan. 2021, Art. no. 015007, doi: 10.1088/1361-665x/abc92d.

[13] Z. Yi, L. Xie, S. Xue, and G. Wan, "A passive wireless acceleration sensing system based on patch antenna and FMCW radar," *IEEE Internet Things J.*, vol. 10. no. 12, pp. 10662–10674, Jun. 2023, doi: 10.1109/JIOT.2023.3240027.

[14] R. Bhattacharyya, C. Floerkemeier, and S. Sarma, "Towards tag antenna based sensing—An RFID displacement sensor," in *Proc. IEEE Int. Conf. RFID*, Orlando, FL, USA, Apr. 2009, pp. 95–102, doi: 10.1109/RFID.2009.4911195.

[15] H. Kou, Q. Tan, Y. Wang, G. Zhang, S. Su, and J. Xiong, "A wireless slot-antenna integrated temperature-pressure-humidity sensor loaded with CSRR for harsh-environment applications," *Sens. Actuators B, Chem.*, vol. 311, May 2020, Art. no. 127907, doi: 10.1016/j.snb.2020.127907.

[16] J. Mahlknecht, G. Wuzella, H. Lammer, and M. Khalifa, "A smart functional surfactant activated conductive polymer coated on paper with ultra-sensitive humidity sensing characteristics," *Mater. Adv.*, vol. 3, no. 3, pp. 1804–1815, 2022, doi: 10.1039/D1MA00740H.

[17] S. Kano and H. Mekaru, "Nonporous inorganic nanoparticle-based humidity sensor: Evaluation of humidity hysteresis and response time," *Sensors*, vol. 20, no. 14, p. 3858, Jul. 2020, doi: 10.3390/s20143858.

[18] B. Tao, L. Feng, F. Miao, and Y. Zang, "High sensitivity chipless RFID humidity sensor tags are based on SnO$_2$/G nanomaterials," *Vacuum*, vol. 202, Aug. 2022, Art. no. 111126, doi: 10.1016/j.vacuum.2022.111126.

[19] A. Ali, S. I. Jafri, A. Habib, Y. Amin, and H. Tenhunen, "RFID humidity sensor tag for low-cost applications," *Appl. Comput. Electromagn. Soc. J.*, vol. 32, no. 12, pp. 1083–1088, 2017.

[20] Y. Feng, L. Xie, Q. Chen, and L.-R. Zheng, "Low-cost printed chipless RFID humidity sensor tag for intelligent packaging," *IEEE Sensors J.*, vol. 15, no. 6, pp. 3201–3208, Jun. 2015, doi: 10.1109/JSEN.2014.2385154.

[21] G. C. Wan, M. M. Li, Y. L. Yang, L. Xie, and L. Chen, "Patch-antenna-based structural strain measurement using optimized energy detection algorithm applied on USRP," *IEEE Internet Things J.*, vol. 8, no. 9, pp. 7476–7484, May 2021, doi: 10.1109/JIOT.2020.3039277.

[22] G. Wan, M. Li, M. Zhang, L. Kang, and L. Xie, "A novel information fusion method of RFID strain sensor based on microstrip notch circuit," *IEEE Trans. Instrum. Meas.*, vol. 71, pp. 1–10, 2022, doi: 10.1109/TIM.2022.3161718.

[23] L. Chen, L. Kang, L. Liu, J. Hu, G. Wan, and L. Xie, "An encoded reconfigurable RFID strain sensor and its information fusion method," *Smart Mater. Struct.*, vol. 31, no. 10, Oct. 2022, Art. no. 105011, doi: 10.1088/1361-665x/ac8b47.

[24] L. Chen, L. Liu, L. Kang, Z. Wan, G. Wan, and L. Xie, "A multibranch U-shaped tunable encoding chipless RFID strain sensor for IoT sensing system," *IEEE Internet Things J.*, vol. 10, no. 6, pp. 5304–5320, Mar. 2023, doi: 10.1109/JIOT.2022.3221938.

[25] Z. Liu, Q. Guo, M. Li, C. Xu, and Y. Li, "Anti-interfering method for environmental foreign bodies for the microstrip antenna sensor," *Measurement*, vol. 195, May 2022, Art. no. 111132, doi: 10.1016/j.measurement.2022.111132.

[26] C. A. Balanis, *Antenna Theory: Analysis and Design*. Hoboken, NY, USA: Wiley, 2016.

[27] M. K. Khandelwal, B. K. Kanaujia, and S. Kumar, "Defected ground structure: Fundamentals, analysis, and applications in modern wireless trends," *Int. J. Antennas Propag.*, vol. 2017, pp. 1–22, Jan. 2017, doi: 10.1155/2017/2018527.

[28] A. Hill and V. K. Tripathi, "Analysis and modeling of coupled right angle microstrip bend discontinuities," in *IEEE MTT-S Int. Microw. Symp. Dig.*, Long Beach, CA, USA, vol. 3, Jun. 1989, pp. 1143–1146, doi: 10.1109/MWSYM.1989.38925.

[29] D. Gopi, A. R. Vadaboyina, and J. R. K. K. Dabbakuti, "DGS based monopole circular-shaped patch antenna for UWB applications," *Social Netw. Appl. Sci.*, vol. 3, no. 2, p. 198, Feb. 2021, doi: 10.1007/s42452-020-04123-w.

[30] Y. Su et al., "Surface acoustic wave humidity sensor based on three-dimensional architecture graphene/PVA/SiO$_2$ and its application for respiration monitoring," *Sens. Actuators B, Chem.*, vol. 308, Apr. 2020, Art. no. 127693, doi: 10.1016/j.snb.2020.127693.

[31] S. Su, W. Lv, T. Zhang, Q. Tan, W. Zhang, and J. Xiong, "A MoS$_2$ nanoflakes-based LC wireless passive humidity sensor," *Sensors*, vol. 18, no. 12, p. 4466, Dec. 2018, doi: 10.3390/s18124466.

[32] F. Deng, Y. He, B. Li, Y. Song, and X. Wu, "Design of a slotted chipless RFID humidity sensor tag," *Sens. Actuators B, Chem.*, vol. 264, pp. 255–262, Aug. 2018, doi: 10.1016/j.snb.2018.02.153.

[33] G. Marchi, V. Mulloni, F. Acerbi, M. Donelli, and L. Lorenzelli, "Tailoring the performance of a Nafion 117 humidity chipless RFID sensor: The choice of the substrate," *Sensors*, vol. 23, no. 3, p. 1430, Jan. 2023, doi: 10.3390/s23031430.

[34] E. Md Amin, N. Karmakar, and B. Winther-Jensen, "Polyvinyl-alcohol (PVA)-based RF humidity sensor in microwave frequency," *Prog. Electromagn. Res. B*, vol. 54, pp. 149–166, 2013, doi: 10.2528/PIERB13061716.